J. Fluid Mech. (2009), *vol.* 638, *pp.* 173–197.
doi:10.1017/S0022112009990498

Jets generated by a sphere moving vertically in a stratified fluid

H. HANAZAKI†, K. KASHIMOTO AND T. OKAMURA

Department of Mechanical Engineering and Science, Kyoto University,
Yoshida-Honmachi, Sakyo-Ku, Kyoto 606-8501, Japan

(Received 15 June 2008; revised 18 May 2009; accepted 18 May 2009; first published online 24 September 2009)

Experiments are performed on the flow past a sphere moving vertically at constant speeds in a salt-stratified fluid. Shadowgraph method and fluorescent dye are used for the flow visualization, and particle image velocimetry is used for the velocity measurement in the vertical plane. Vertical 'jets' or columnar structures are observed in the shadowgraph for all the Froude numbers $Fr (0.2 \lesssim Fr \lesssim 70)$ investigated, and the wake structures in the whole parameter space of Fr and the Reynolds number $Re (30 \lesssim Re \lesssim 4000)$ are classified into seven types, five of which are newly found. Those include two types of thin jets, one of which is short with its top disturbed by internal waves to have a peculiar 'bell-shaped' structure, while the other has an indefinitely long length. There are two other new types of jet with periodically generated 'knots', one of which is straight, while the other has a spiral structure. A simply meandering jet has also been found. These wake structures are significantly different from those in homogeneous fluids except under very weak stratification, showing that the stratification effects on vertical motion are much more significant than those on horizontal motion.

1. Introduction

Stratified flows have been studied mostly for horizontal mean flows (Hunt & Snyder 1980; Hanazaki 1988), since many applications have been limited to large-scale atmospheric and oceanic flows, where horizontal component of velocity is much larger than the vertical component. On the other hand, vertical mean flows, or the flows generated by a vertically moving obstacle, would be important in smaller-scale phenomena, such as the control of vertical movement of buoys used for the oceanic observation and the prediction of the vertical movement of planktons.

Buoys used for the ocean observation, such as Lagrangian floats, are generally designed to move along the mean flows in the deep ocean, to measure the local temperature and salinity. The mean flows are predominantly horizontal, but vertical motion is essential when they periodically move up to the sea surface to send their observed data to the satellite and go back to the prescribed depth (e.g. D'Asaro 2003). Zooplanktons, such as Copepoda, carry the protein and carbon in the ocean and play one of the major roles in the carbon cycle of the ocean. Therefore, fundamental analysis of their vertical movement in stratified environment would be of much use for modelling the carbon cycles in the ocean.

† Email address for correspondence: hanazaki@mech.kyoto-u.ac.jp

Specifically, in the slow vertical motion of Lagrangian floats (vertical velocity $W = 1\,\mathrm{cm\,s^{-1}}$) with an oceanic value of the Brunt–Väisälä frequency $N = 0.01\,\mathrm{s^{-1}}$ and a typical size of float $L = 100\,\mathrm{cm}$, the Froude number $Fr = W/NL$ and the Reynolds number $Re = WL/\nu$ ($\nu \sim 0.01\,\mathrm{cm^2\,s^{-1}}$ is the dynamic viscosity of water $^{-1}$) become $Fr \sim 1$ and $Re \sim 10^4$ (cf. § 6 of D'Asaro 2003), while in the case of a large zooplankton with a size of $L \sim 1\,\mathrm{cm}$ and a mean vertical velocity $0.01\,\mathrm{cm\,s^{-1}}$, these parameters become $Fr \sim 1$ and $Re \sim 1$. These parameter values would be accessible by laboratory experiments or numerical studies.

However, there have been only a few studies on the vertically moving obstacles in stratified fluids. The first study would be traced back to Mowbray & Rarity (1967), in which the large-scale patterns of internal gravity waves generated by a vertically moving sphere have been investigated by means of a Toepler schlieren system. They found lee-wave patterns which agree with the linear wave theory. It is of interest to note that some of their photographs simultaneously show vertical jet-like structures on the centre axis of the flow, although they did not give any comments on it.

The near-wake structure of a vertically moving sphere was first investigated by Ochoa & Van Woert (1977), who mainly used shadowgraph technique. They found two new types of wakes, namely a vertical columnar structure (type C in this paper; cf. figure 5*c*) at relatively low Froude and Reynolds numbers and a turbulent wake (type G; cf. figure 5*g*) at large Froude and Reynolds numbers. These jet-like structures are remarkably different from those in homogeneous fluid, showing strong effects of stratification on vertically moving obstacles. In the meanwhile, their experimental methods would require improvements, since the vertical-density gradient was not uniform and uncertainties existed in the values of Brunt–Väisälä frequency. The method of towing a sphere would also require revision. In their experiments, the sphere was towed by a vertically spanned wire. However, more recent studies for a horizontally moving sphere show strong effects of the boundary layer generated on the pulling rod or wire spanned along the moving direction of the obstacle (e.g. Lin *et al.* 1992; Chomaz, Bonneton & Hopfinger 1993). In the case of a vertically moving sphere, the problem would be more serious, since a rear jet is formed on the vertical symmetry axis, and the boundary layer would affect the wake structure significantly.

In the experiments of a freely falling small particle (0.25–1.8 mm in diameter) across a density interface, Srdić-Mitrović, Mohamed & Fernando (1999) found that the particle pulls the upper-layer fluid into the lower layer and generates a fluid column on its rear side, resulting in significant increase of drag force. The phenomenon has similarity to the jet observed in continuously stratified fluid. Abaid *et al.* (2004) observed the vertical buoyancy oscillation of a freely falling small sphere and compared the results with the solution of model equations.

In a numerical study, Torres *et al.* (2000) investigated the axisymmetric flow around a vertically moving sphere mainly at moderate Reynolds numbers ($50 \leqslant Re \leqslant 200$). They found that the columnar structure found by Ochoa & Van Woert (1977) is indeed a vertical round jet whose maximum velocity increases up to about 10 times that of the sphere velocity and identified significant increase of the drag accompanying the jet formation. For example, the drag coefficient increases up to $C_D \sim 21$ at $Re = 100$, about 20 times larger compared to its unstratified value ($C_D \sim 1.1$).

In this study we have visualized the wake of a vertically moving sphere under uniform density stratification with a newly developed method of vertical towing and investigated the wake patterns for a much wider range of the Reynolds number and Froude number than previous experiments. We will confirm by velocity measurements (through particle image velocimetry or PIV) that the columnar structure observed by

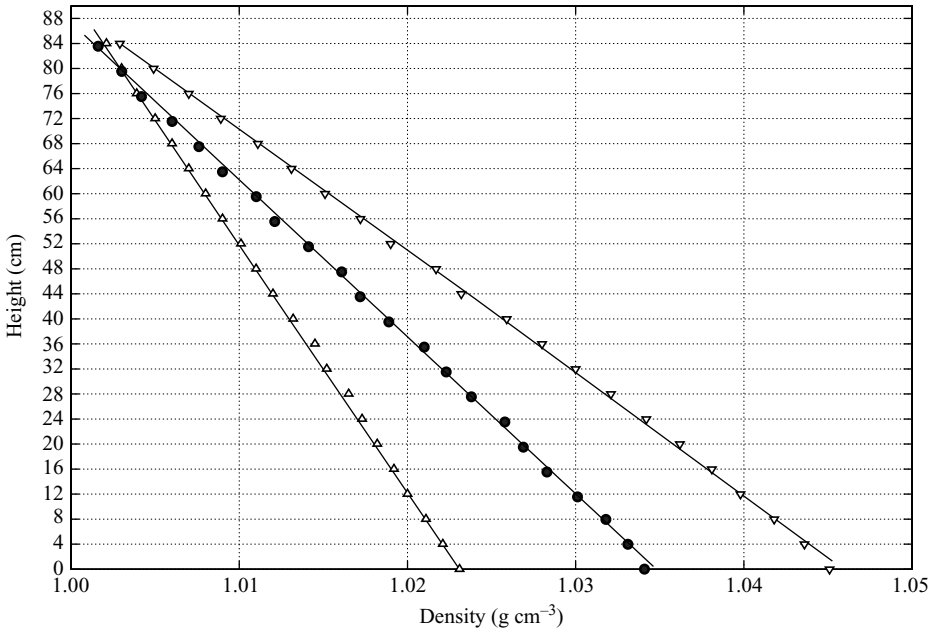

FIGURE 1. Typical mean-density distributions in the test tank. The height is measured from the bottom of the tank. The symbols are as follows: $\triangle$, $N = 0.49\ \mathrm{s}^{-1}$; $\bullet$, $N = 0.62\ \mathrm{s}^{-1}$; $\triangledown$, $N = 0.70\ \mathrm{s}^{-1}$.

shadowgraph is actually a vertical jet, at least when the stratification is moderate or strong.

2. Experiments

The experiments were performed in a test tank with horizontal dimension of $80 \times 80\,\mathrm{cm}^2$ and height of 94 cm. Stratified salt water (Schmidt number $Sc \sim 700$) is generated in the tank by the two-tank method. Namely pure water is pumped in initially; then increasingly denser salt water is pumped in by a metering pump (maximum $7.2\,\mathrm{L\,min}^{-1}$) from the bottom of the tank. A circular stainless plate 12 cm in diameter is fixed at $5 \sim 8$ mm from the tank floor just above the inlet of the fluid, so that the fluid flows into the tank horizontally. The tank is finally filled up to the height of $H = 85$ cm from the bottom. Three of the four sidewalls of the test tank are made of glass, while one of them is acrylic so that many small cocks could be easily attached to the wall at the vertical interval of 4 cm. Small amount of fluid is released horizontally from these cocks according to the mechanism of selective withdrawal, and fluid density is measured by two refractometers. One is Atago ATC-S/Mill-E (accuracy: $\pm 0.001\,\mathrm{g\,cm}^{-3}$) which transforms the refractive index to salinity and density automatically, and the other is Reichert AR200 (accuracy: ± 0.0001 in refractive index) which is used simultaneously for low N ($\lesssim 0.3\,\mathrm{s}^{-1}$). Both refractometers can compensate for the temperature variation. Some examples of the vertical-density distribution obtained by this procedure are shown in figure 1, where the Brunt–Väisälä frequency, N, is defined by $N = (-(g/\rho_0)\mathrm{d}\overline{\rho}/\mathrm{d}z)^{1/2}$ (ρ_0 is the representative density, $\overline{\rho}(z)$ the unperturbed density distribution, g the acceleration due to gravity and z the vertical coordinate).

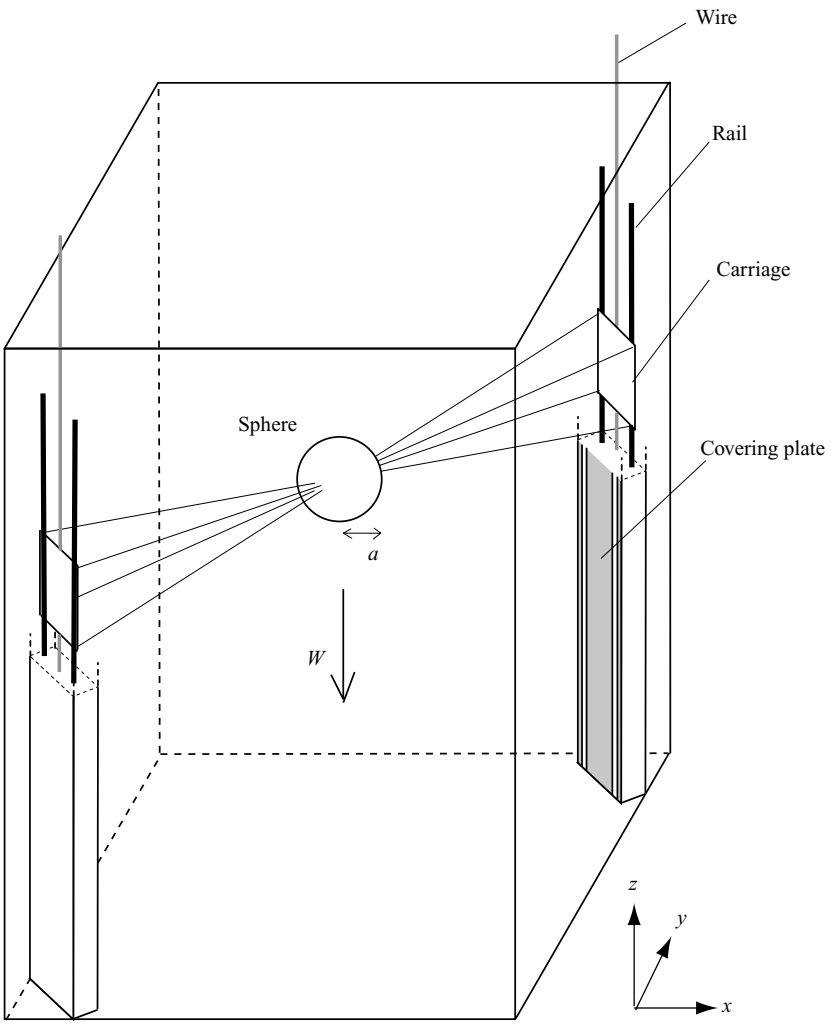

FIGURE 2. Schematic figure of the test tank.

An acrylic sphere is moved vertically at a constant speed W in the range of $0.5 \leqslant W \leqslant 10$ cm s^{-1}, using a high-torque DC motor. The sphere is sustained by eight very thin stainless-steel wires of 0.1 mm in diameter (figure 2). These wires are spanned obliquely across the tank through the centre of the sphere and do not disturb the flow near the vertical symmetry axis of the flow, with no boundary layers on that axis. We first tested the usage of a vertical towing wire, but it actually produced a boundary layer on its surface. The most serious shortcoming of this method is the difficulty of discerning the shadowgraph image of real vertical jet from that of the boundary layer around the wire. They both appear on the vertical symmetry axis of the flow, and the boundary layer continues to develop for an indefinitely long distance and overlaps the real jet. This inhibits the observation of thin and short jets (cf. figure 5*a*) in particular. Another shortcoming of this towing method is that the sphere inevitably rotates around the wire irregularly as it goes up and down. This would affect the flow patterns, especially when the flow is unsteady and non-axisymmetric.

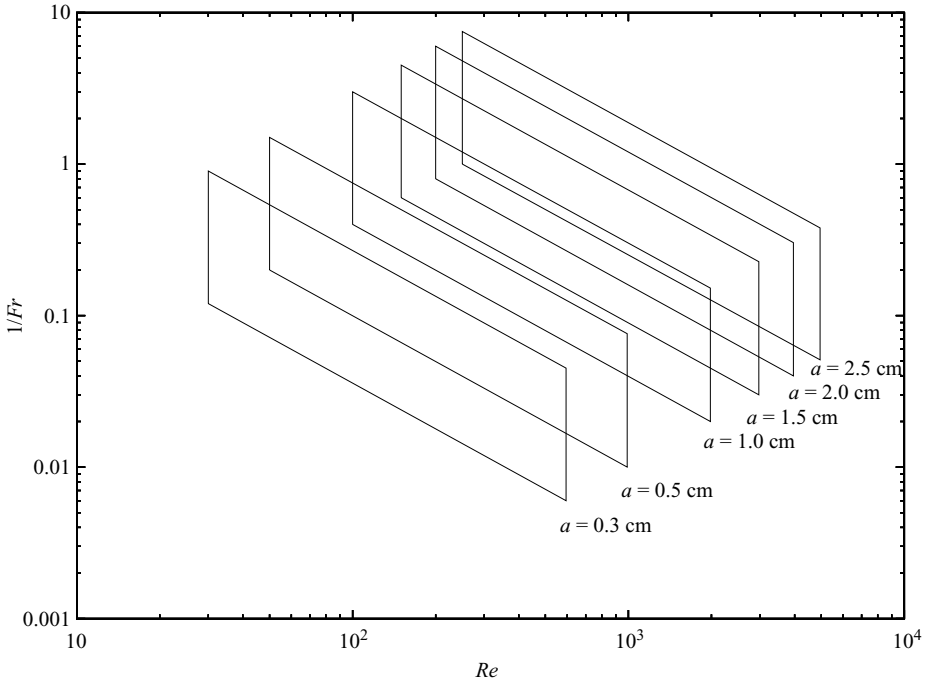

FIGURE 3. The parameter range $(Re, 1/Fr)$ achievable using six sizes of the sphere (radius $a = 0.3$, 0.5, 1.0, 1.5, 2.0, 2.5 cm), varying N (0.2 rad $s^{-1} \leqslant N \leqslant 1.6$ rad s^{-1}) and W ($0.5\,\mathrm{cm\,s^{-1}} \leqslant W \leqslant 10\,\mathrm{cm\,s^{-1}}$).

The obliquely spanned wires resolve both of these two problems, and similar methods have been used in studies for a horizontally moving sphere (Lin *et al.* 1992; Chomaz *et al.* 1993; Spedding, Browand & Fincham 1996).

For the smooth vertical movement of a sphere, we have connected a carriage (moving flat plate) to vertical rails (figure 2) by small sliders made of polytetrafluoroethylene (PTFE), usually called Teflon, so that the friction becomes sufficiently small and the carriage works well even in salt water. The carriage is fluid dynamically insulated from the main body of fluid by a covering plate, so that its movement would not affect the fluid motion near the sphere at the centre of the tank.

Six spheres with radii $a = 0.3$, 0.5, 1.0, 1.5, 2.0 and 2.5 cm are used for the experiments. The radius a, together with the Brunt–Väisälä frequency, N, and the vertical velocity, W, of the sphere, determines the observable parameter regions $(Re, 1/Fr)$, where the Reynolds number and the Froude number are defined by $Re = W(2a)/\nu$ (ν is the dynamic viscosity coefficient) and $Fr = W/Na$. Figure 3 shows the parameter region achievable against the full range of $0.2 \leqslant N \leqslant 1.6$ rad s^{-1} and $0.5 \leqslant W \leqslant 10\,\mathrm{cm\,s^{-1}}$. Each parallelogram corresponds to one size of the sphere, and the variation of $1/Fr$ along the ordinate is realized by changing N in the experiments, while the variation parallel to the top or bottom side of each parallelogram is realized by changing W.

The horizontal size of the tank is large enough to minimize the sidewall effects. Even if we use the maximum size of the sphere ($a = 2.5$ cm), the ratio to the tank width is only $2a/80\,\mathrm{cm} = 0.06$. This value is much smaller than the previous experiments for horizontal flows in which the maximum ratio was typically $0.15 \sim 0.25$.

Sufficiently long duration of steady movement of a sphere is necessary to reach a stationary state of the flow. The condition is usually given by $Wt_{max}/2a \gtrsim 10$, i.e. $t_{max} \gtrsim 20a/W$. Since the maximum duration time t_{max} is given by H/W in the present case, the condition is rewritten as $H \gtrsim 20a$. Since the fluid depth is $H = 85\,\mathrm{cm}$, this condition is satisfied for all the sphere sizes ($a_{max} = 2.5\,\mathrm{cm}$). Another necessary condition comes from the fact that sufficient time is necessary before stratification becomes effective. This second condition would be given by $Nt_{max} \gtrsim 1$ (e.g. Lin *et al.* 1992), which is rewritten as $1/Fr \gtrsim a/H$. For example when $H = 85\,\mathrm{cm}$ and $a_{max} = 2.5\,\mathrm{cm}$, $1/Fr \gtrsim 0.03$. Since smaller value of $1/Fr$ is possible for smaller spheres, this condition is satisfied for all the cases investigated in this study (cf. figure 3).

Standard shadowgraph technique is applied to many of the parameters $(Re, 1/Fr)$ investigated, using a 220 W DC lamp as a light source. A translucent white acrylic sheet of 1 mm thickness is used as a screen to be photographed by a digital single-lens reflex camera (Canon EOS 30D) from the other side of the test tank. Since the shadowgraph represents the second derivative of density in space, it is a very sensitive visualization method, but obtained images give only the integrated effects along the path of light. To complement this, two other visualization methods have been also used for several sets of parameters $(Re, 1/Fr)$.

In this study fluorescein sodium (or uranine) is used for the dye visualization. It is released from the vicinity of upstream stagnation point of the sphere by injecting a drop of strong solution of dye using a syringe. The dye visualizes flows near the sphere surface and along the rear vertical axis of the flow.

PIV is also used for several typical sets of (Re, Fr) to measure the velocity field in the vertical jet and to compare results with the corresponding shadowgraph images. Double-pulsed Nd:YAG laser (Dual Power 65-15, Dantec Dynamics; Nano S PIV, Litron Lasers; 532 nm, 65 mJ, 15 Hz) is used to produce a vertical light sheet of $\sim$1 mm in thickness. The relaxation time of small tracer particles (white watercolour pigment), necessary to attain the fluid velocity, can be estimated by $\tau_s = d_p^2 \rho_p / 18\mu$, where d_p is the diameter, ρ_p is the density of tracer particles and μ is the viscosity coefficient of fluid. In the present experiments, $d_p \sim 100\,\mathrm{nm}$, $\rho_p \sim 1.5\,\mathrm{g\,cm^{-3}}$ and $\mu \sim 0.01\,\mathrm{g\,cm^{-1}\,s}$, giving the relaxation time as $\tau_s = 0.6\,\mathrm{ns}$. This value is negligibly small compared to the typical time scale of the flow, assuring the passive movement of the seeding particles. The steady descending velocity W_p of the particle can be estimated by the balance among the gravity force, the buoyancy force and the Stokes drag as $W_p = (d_p^2 g/18\mu)(\rho_p - \rho_f)$, where ρ_f is the fluid density. Substituting the minimum value of $\rho_f = 1\,\mathrm{g\,cm^{-3}}$ (pure water) at the top of the stratified water, the maximum value of $W_p = 6 \times 10^{-9}\,\mathrm{m\,s^{-1}}$ is obtained. Therefore, there is almost no movement of particles when the sphere is stationary. To observe the particle movement, a CCD camera with the resolution of 2048×2048 pixels (HiSense 4M, Dantec Dynamics; C9300-501, Hamamatsu Photonics; 12 bits, 11 Hz) is used, in combination with a 60 mm objective lens (AF Micro-Nikkor 60 mm f/2.8D, Nikon). The observed vertical domain, just above the sphere when it is going down, has the dimension of approximately 20 cm $\times$ 20 cm, and the adaptive cross-correlation was used to analyse the particle images.

Refractive-index matching (McDougall 1979; De Silva & Fernando 1998) is not performed in this experiment, since it makes shadowgraph visualization impossible. The change of refractive index in the vertical direction due to the salt stratification can be estimated as follows. When the concentration of salt is x g $\mathrm{L^{-1}}$, the refractive index n of salt water at 21°C becomes

$$n = 1.3329 + 1.71 \times 10^{-4} x. \tag{2.1}$$

Since the vertical difference of x in the PIV measurements in this study for $N = 0.6\,\mathrm{s}^{-1}$ (type A in figures 10 and 11) and maximum moving range of the sphere ($\sim$70 cm) is $\Delta x \sim 26\,\mathrm{g\,L}^{-1}$, the difference in n is $\Delta n \sim 0.0044$. Then, the value of n changes at most by 0.33 %, and it will lead to the maximum possible errors in the vertical position and the velocity of particles at the same rate. Therefore, the measurement errors would be fairly small. The accuracy of the velocity measurement would also be supported by the agreement with numerical simulations (cf. figures 11*a* and 12).

3. Results

All the parameters (Re, $1/Fr$) investigated by the shadowgraph technique are plotted in figure 4(*a*). The parameter range is much wider than that in Ochoa & Van Woert (1977), where the range of $200 \leqslant Re \leqslant 4000$ and $3.77 \leqslant Fr \leqslant 35$ ($0.028 < 1/Fr < 0.265$) has been investigated (cf. figure 2 of Torres *et al.* 2000). In the present study the parameter region is found to be divided into seven regions (A $\sim$ G).

Since a practically interesting phenomenon of significant drag increase has been observed in the vertical motion of an obstacle in stratified fluids, numerically obtained increase of drag coefficient C_d at $Re = 200$ and $Sc = 700$ is shown in figure 4(*b*) (from Hanazaki, Konishi & Okamura 2009*b*). This shows that, in figure 4(*a*) with a fixed value at $Re = 200$, drag coefficient increases significantly as $1/Fr$ increases and the flow pattern changes from type C to type A.

Typical shadowgraph images in all the regions (A $\sim$ G) are given in figure 5. Dye visualizations are also performed for types A, C and G as described in figures 6 and 7. All the shadowgraph photographs shown in this paper are taken when the sphere is descending. When the sphere is ascending, the black region reverses into white and vice versa, since the density perturbation would have the opposite sign. Note that the flow patterns essentially do not depend on whether the sphere is descending or ascending, as long as the density stratification is not too strong and the Boussinesq approximation can be applied. This could be actually confirmed in the present experiments even for the strongest stratification ($Fr \sim 0.2$, $N = 1.6\,\mathrm{s}^{-1}$).

Type A (figure 5*a*), which has a thin jet, occurs generally at strong stratification ($Fr \lesssim 3$; cf. figure 4). The top of the jet is bounded by a peculiar bell-shaped region which appears in this figure at about 3*a* above the rear stagnation point of the sphere. Above the bell-shaped region, the jet becomes unstable and meanders, breaking into small turbulent eddies. It would be of interest to note that the bell moves with the sphere at a constant speed without changing its relative position to the sphere. This steadiness, as shown below (see figure 13), is related to the fact that the bell is a result of steady lee waves excited by the sphere; i.e. the phase velocity of the bell agrees with the sphere velocity.

The vertical centre axis in the rear of the sphere looks dark. This can be explained in combination with the previous numerical results (Torres *et al.* 2000). The fluid on the centre axis has been originally pulled downward from the upper region of the test tank in which the fluid density is low, and thus the refractive index is also low. Then, when the light fluid goes back to its original height due to the buoyancy force, its refractive index is smaller than the surrounding fluid. Therefore, when the external light horizontally approaches the centre axis of the flow, it horizontally deflects away from the axis, allowing small amount of light to pass through the centre axis. This explains why the rear axis looks dark. Conversely, when the sphere is ascending, the centre axis becomes bright.

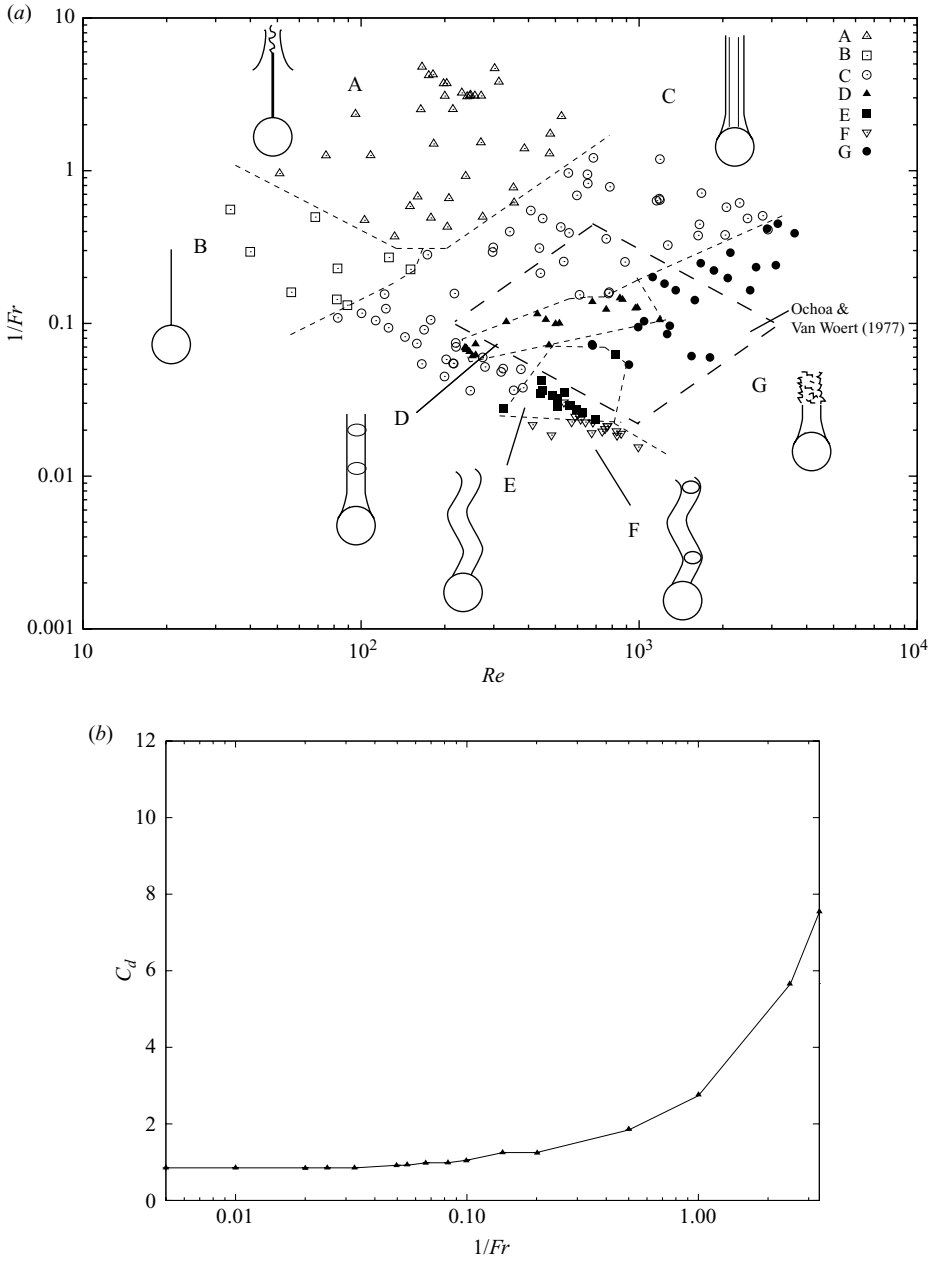

FIGURE 4. (*a*) The parameter range (Re, $1/Fr$) investigated in the experiments; A $\sim$ G denote the regions in which wake patterns A $\sim$ G (cf. figure 5) have been observed. (*b*) The drag coefficients at $Re = 200$ obtained by numerical simulations (Hanazaki *et al.* 2009*b*).

In the dye visualization (figure 6(*a*), $Re = 230$, $Fr = 0.30$), meandering of the thin jet is clearly observed, but the bell-shaped pattern is not discernible, although the pattern is clearly observed in PIV and shadowgraph results at similar parameters (cf. figure 5(*a*), $Re = 199$, $Fr = 0.32$; figure 10(*a*, *b*), $Re = 247$, $Fr = 0.32$). This shows that the bell does not consist of fluid which originates from the points near the upstream

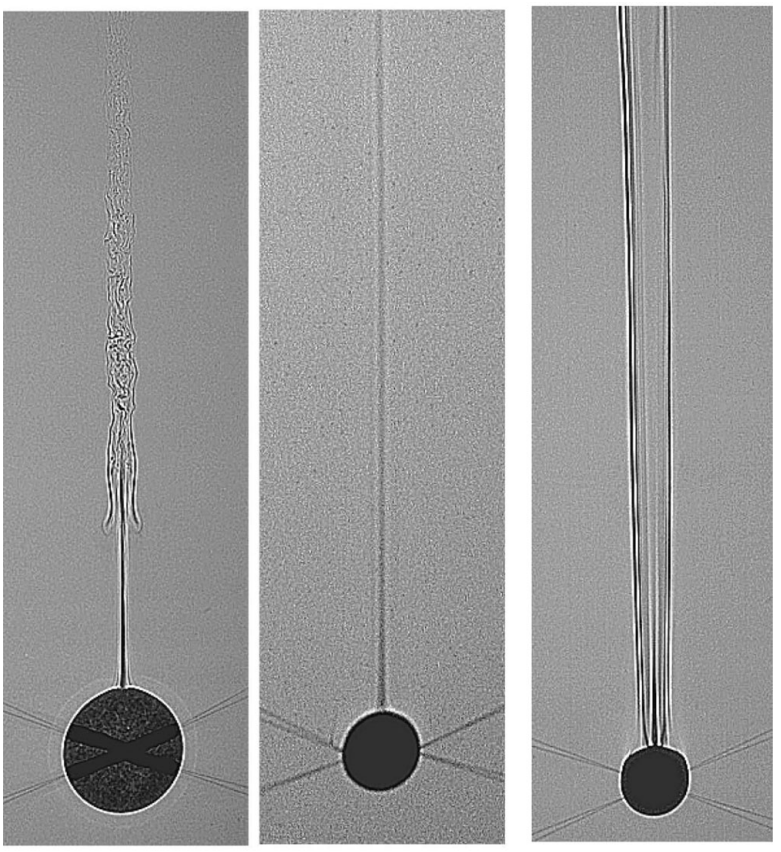

FIGURE 5. For legend, see next page.

stagnation point of the sphere. Indeed, when we initially place dyes at much wider regions ahead of the sphere, some of the dyes form a bell-shaped pattern (figure 7). This supports the conjecture that the bell would be the direct consequence of the internal waves and not of the jet.

Type B (figure 5*b*), which appears at weaker stratifications than type A, is an indefinitely long and straight thin jet. In the shadowgraph image, there is only one black line on the vertical symmetry axis. Major differences from type A are that there is no bell-shaped region and no instability or meandering of jet. Both in type A and B, thickness T of the central dark region of thin jet did not show any clear dependence on Fr or Re, and it was in the range of $0.025 < T/2a < 0.12$. The value can be altered by the Brunt–Väisälä frequency, N, even for the same Re and Fr, i.e. for the same flow pattern, since the refractive index can change solely by N, and the dark region appears due to the mechanisms as described above.

Type C (figure 5*c*) is a long broad jet with multiple vertical black lines in the shadowgraph image. The width of jet generally increases as the stratification becomes weaker, as will be shown later in figure 15. The structure of type C might be more clearly observed in dye visualization (figure 6*b*) with some hints of three-dimensional structure. On the rear axis of the flow, the concentration of dye is large and looks yellow, and the yellow region is surrounded by a green region with less dye

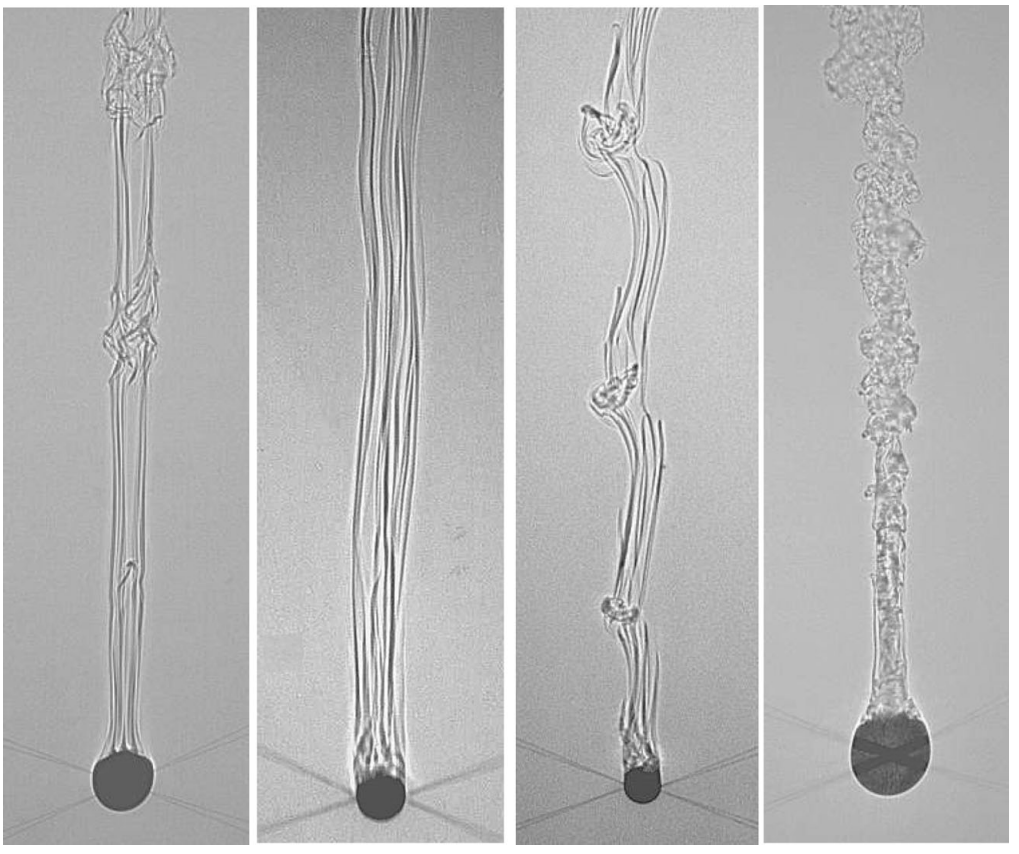

FIGURE 5. The shadowgraph images of type A ~ G. The values of (Re, Fr) are (*a*) type A, (199, 0.32); (*b*) type B, (126, 3.7); (*c*) type C, (610, 6.5); (*d*) type D, (678, 7.2); (*e*) type E, (567, 34.6); (*f*) type F, (589, 40.6); (*g*) type G, (2637, 4.3).

concentration. A close look at the photograph near the rear stagnation point suggests that the surrounding green region is not axisymmetric at this large Reynolds number ($Re = 1189$), probably with a starfish structure in the horizontal plane, although the number of 'legs' of the starfish is uncertain, and more detailed investigation is necessary.

It is also of interest to note that much more amount of dye is observed in type C (figure 6*b*) around the sphere surface and in the wake region compared to type A (figure 6*a*), even though the total amount of dye used for each visualization is comparable. A probable explanation is that in type A, most of the dragged light fluid goes back to its original height before the sphere comes down to the illuminated area in which the photograph was taken, while in type C, much of the dragged fluid still resides near the sphere. Indeed in type A, the dye concentration around the sphere significantly decreases as the sphere descends, while in type C only slight reduction has been observed. In other words, the isopycnals are cut away by diffusion in type A, while they deform continuously in type C. This would occur since the diffusion effect in the wake region is weaker in type C, due to the smaller density gradients.

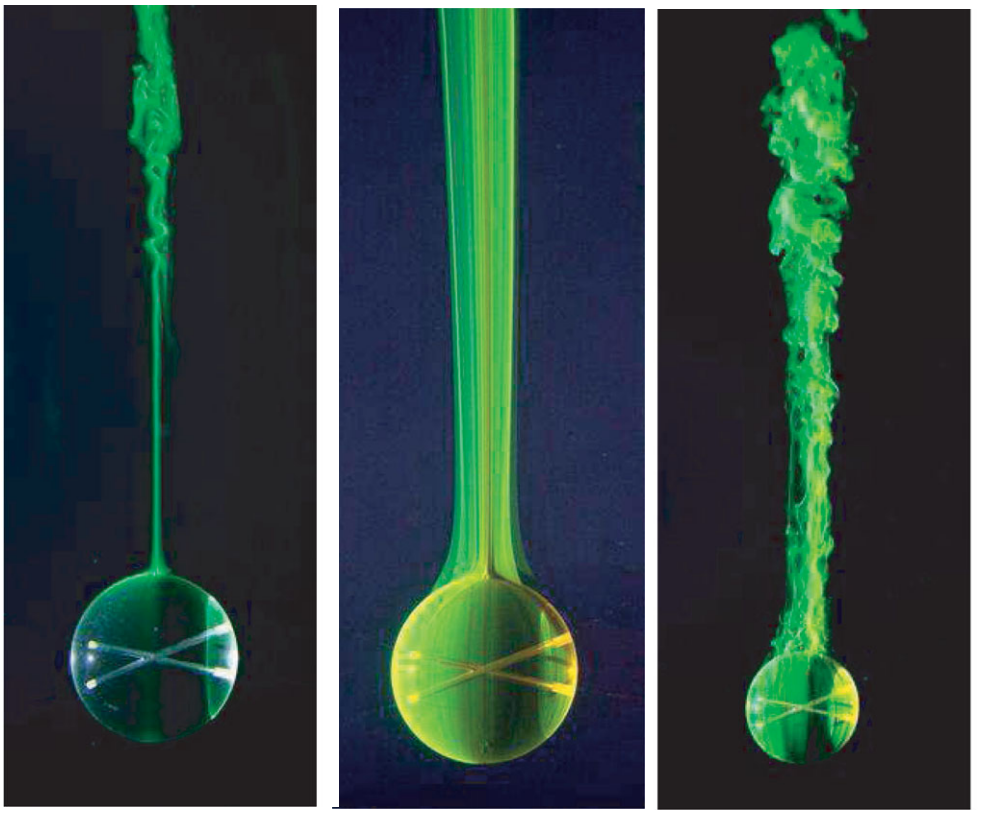

(*a*) (*b*) (*c*)

FIGURE 6. The dye visualization of the wake structures of types A, C and G. The values of (*Re*,*Fr*) are as follows: (*a*) type A, (230,0.30); (*b*) type C, (1189,1.55); (*c*) type G, (3101,4.17).

Details of these processes, including the difference between types A and C, can be investigated by numerical simulations (Hanazaki, Kashimoto & Okamura 2009*a*).

Type D (figure 5*d*) is also a broad straight jet, but it is unsteady with periodic generation of knots. The knots slowly move upward when the sphere goes down, and the generation period increases with the Froude number as will be shown later in figures 16 and 17. Type E (figure 5*e*) is a slightly meandering broad jet without knots, while type F (figure 5*f*) is another jet with periodic knots but has a spiral structure, with the position of knots off the symmetry axis of the flow. Finally type G (figure 5*g*, 6*c*) is a turbulent jet which appears at high Reynolds numbers.

The length of jet in type A, defined here as the distance from the rear stagnation point of the sphere to the lowest end of the bell-shaped region, increases with *Fr* as shown in figure 8. For the strongest stratification (figure 8*a*, same as figure 5*a*), clear bell-shaped region can be observed, while the shape deforms when it moves away from the sphere as the Froude number becomes larger. Similar bell-shaped region appears also in type C (figure 9). Although the radius of the jet is larger and the deformation of the bell-shaped region is more significant, the length of jet again increases with *Fr*, showing a similar influence of stratification.

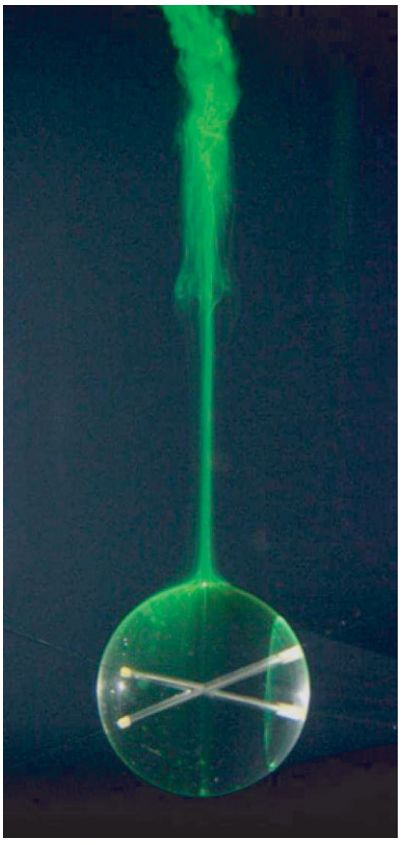

FIGURE 7. The dye visualization of the wake structures of type A, when the dye exists initially in a wide region ahead of the sphere. The parameter values are similar to figure 6(*a*), i.e. $(Re, Fr) = (245, 0.30)$.

Froude-number dependence of the jet length for types A and C ($L_A/2a$, $L_C/2a$) is plotted in figure 10. The plots approximately follow a line of proportionality,

$$L/2a = 3Fr, \tag{3.1}$$

independent of the Reynolds number, although the proportionality constant tends to decrease at large Fr for type C. This suggests that the appearance of bell-shaped region is a result of stratification, with little effects of viscosity and diffusion. Indeed, the relation can be rewritten as $L \sim 6W/N$, showing that the jet length is determined only by N and W. The independence from the sphere size a and the viscosity means that the effect of the surface boundary layer is minor.

It would be of interest here to consider the linear theory for internal gravity waves. The theory tells that the lines of constant phase far from the obstacle are described by (Mowbray & Rarity 1967; Torres *et al.* 2000)

$$r/2a = \frac{1}{2} Fr \Phi \left(\frac{(\sigma^{-4} + \sigma^{-2} - 1)(1 - \sigma^2)^3}{(1 - \sigma^2)^3 + \sigma^2 (2 - \sigma^2)^2} \right)^{\frac{1}{2}}, \tag{3.2}$$

$$z/2a = \frac{1}{2} Fr \Phi \sigma (2 - \sigma^2) \left(\frac{\sigma^{-4} + \sigma^{-2} - 1}{(1 - \sigma^2)^3 + \sigma^2 (2 - \sigma^2)^2} \right)^{\frac{1}{2}}, \tag{3.3}$$

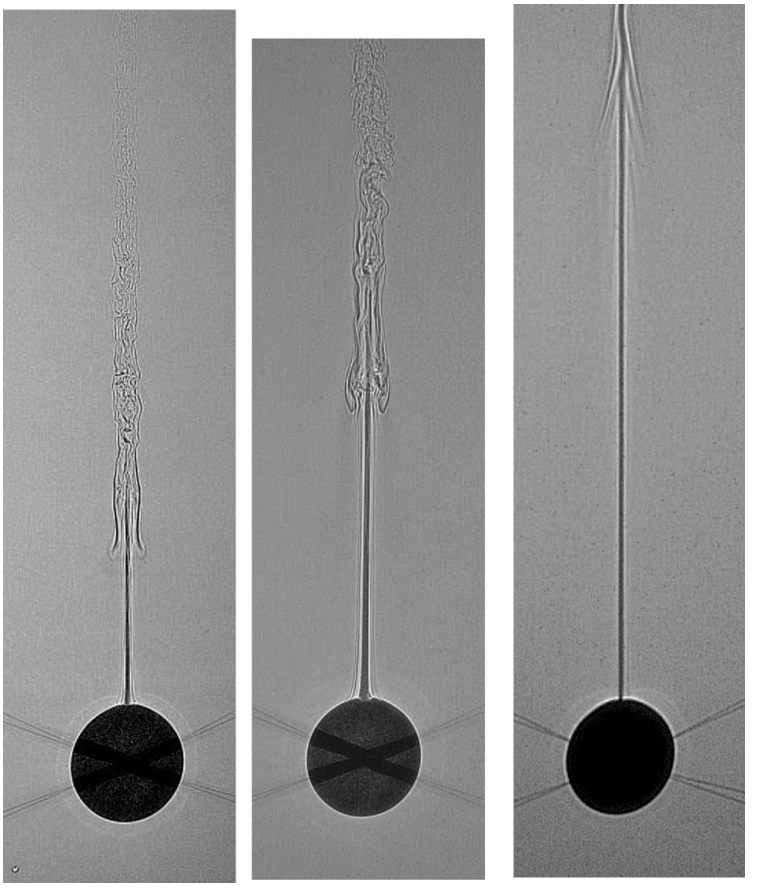

(*a*) (*b*) (*c*)

FIGURE 8. Variation of the length of jet for type A. The length is limited by the generation of a bell-shaped region on the symmetry axis of the flow. (*a*) $(Re, Fr) = (199, 0.32)$; (*b*) $(Re, Fr) = (476, 0.77)$; (*c*) $(Re, Fr) = (206, 1.5)$.

where σ $(0 < \sigma < 1)$ is a variable parameter; Φ is the phase of internal wave; and $\Phi = (n - 1/4)\pi$ $(n = 1, 2, \ldots)$ corresponds to $w = 0$. On the vertical symmetry axis at which $r \to 0$, (3.2) gives $\sigma \to 1$ so that (3.3) gives the corresponding vertical coordinate as $z/2a = Fr\Phi/2$. Then, $w = 0$ occurs at $z/2a = Fr(n - 1/4)\pi/2$ $(n = 1, 2, \ldots)$, giving the distance between the lines of constant phase as

$$\Delta z/2a = \pi Fr/2 \ (\sim 1.5Fr). \tag{3.4}$$

Although this result is applicable only to the far field and quantitative comparison with the experimental results near the sphere may not be adequate, the proportionality to Fr agrees with the behaviour of the jet length, suggesting that the position of the bell-shaped region is determined by the internal waves. Numerical simulations by Torres *et al.* (2000) similarly show that the vertical distance between the lines of constant phase near the sphere is considerably underestimated by the linear theory.

This could indeed be confirmed by the velocity distributions obtained by the PIV measurements. Figure 11(*a*) shows the velocity distribution in the vertical plane across the centre of the sphere, and figure 11(*b*) shows the shadowgraph image at the same

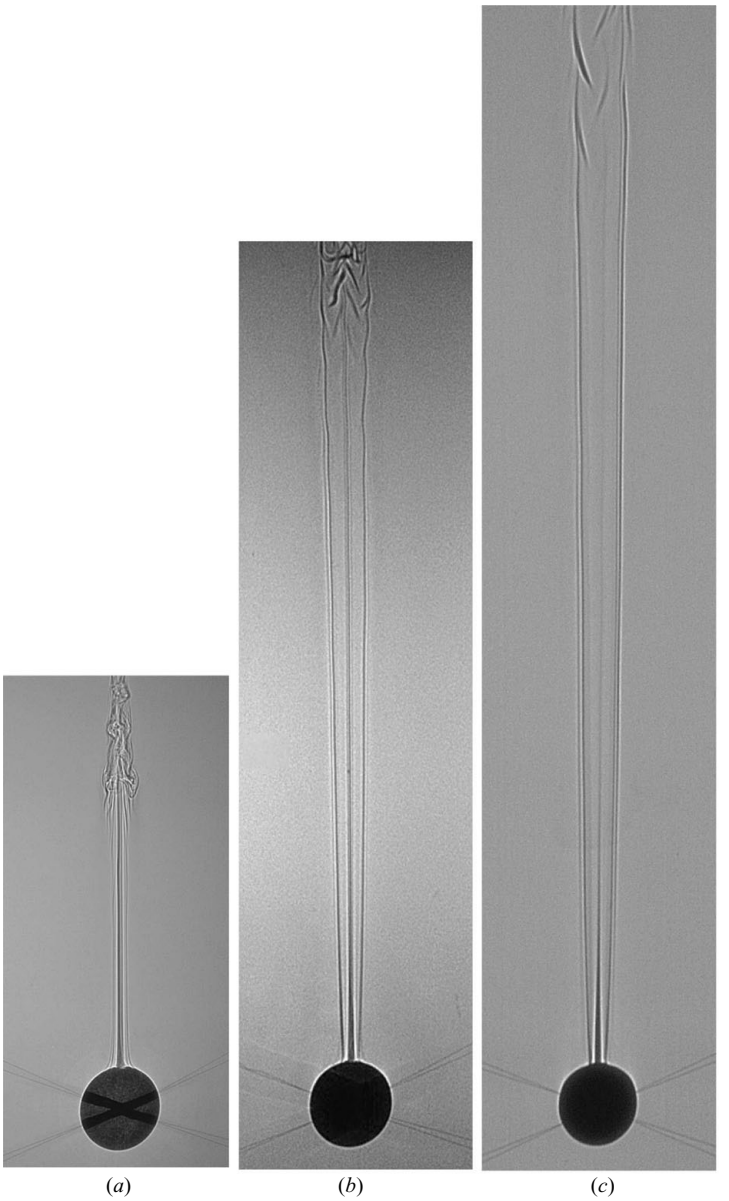

FIGURE 9. Variation of the length of jet for type C. (*a*) $(Re, Fr) = (652, 1.05)$; (*b*) $(Re, Fr) = (761, 2.8)$; (*c*) $(Re, Fr) = (441, 4.7)$.

set of parameters ($Re = 247$, $Fr = 0.32$). First, the PIV results verify the existence of a 'jet' in the vertical columnar structure observed by the shadowgraph. The jet has been identified by numerical simulations (Torres *et al.* 2000) but has not yet been observed in the experiments. At the same time, we note that the bell-shaped pattern in the shadowgraph is adjacent to a descending flow around the jet, and the velocity distributions in general have diverging patterns similar to the linear theory (Lighthill 1978), schlieren photographs (Morbray & Rarity 1967) and numerical simulations (Torres *et al.* 2000).

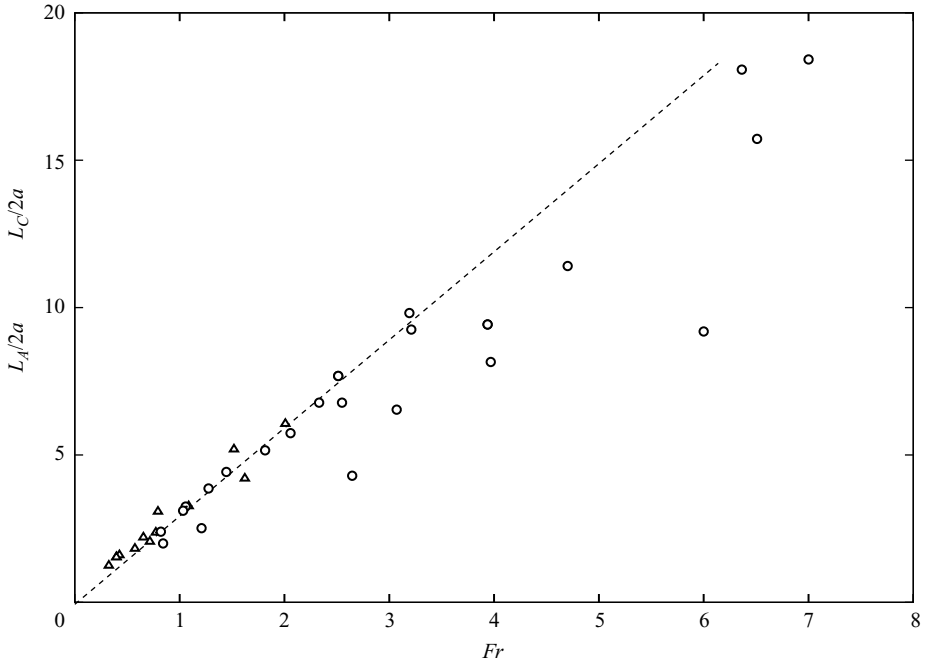

FIGURE 10. Froude-number dependence of the length of jet in types A and C: △ denotes type A ($L_A/2a$) and ○ denotes type C ($L_C/2a$). The dashed line denotes the relation $L/2a = 3.0Fr$.

To check the accuracy of the velocity distributions obtained by PIV, we show the results of numerical simulations at the same parameters in figure 12 (Hanazaki *et al.* 2009*a*). Details of the numerical methods are described in Hanazaki *et al.* (2009*b*). Strong similarity of the velocity distributions in the jet and the generation of the downward velocity in the bell-shaped region illustrate the accuracy of the PIV results.

To identify these wave patterns clearly, contours of the vertical velocity w are drawn in figure 13. Typical patterns of diverging internal waves are observed in the contours of $w = 0$, but the uppermost contour of $w = 0$ deforms along the bell-shaped pattern. Therefore, we conclude that the bell-shaped pattern has its origin in internal gravity waves. Namely the internal waves induce descending fluid motion (the dashed lines in figure 13) around the ascending jet ($w_{max} \sim 5.6W$), generating a stagnant bell-shaped region.

It would be appropriate here to discuss the transition between types A and B. As Fr increases, the distance of bell-shaped pattern from the sphere increases in proportion to Fr, and the internal-wave amplitude decreases due to the diverging effects and the viscous dissipation. On the other hand, as Re decreases, the velocity and density perturbations dissipate faster due to stronger viscous/diffusive effects. These two effects are consistent with the fact that the borderline between types A and B in the $(Re, 1/Fr)$ map runs from upper left to lower right (figure 4*a*).

However, there are some ambiguities in the position of the borderline, since there would be several other reasons for the disappearance of the bell-shaped pattern, other than the values of Re and Fr. One possible reason is that the bell becomes so remote from the sphere that it no longer appears in the test tank. This would occur when

$$L_A \sim 3Fr \times 2a > H, \tag{3.5}$$

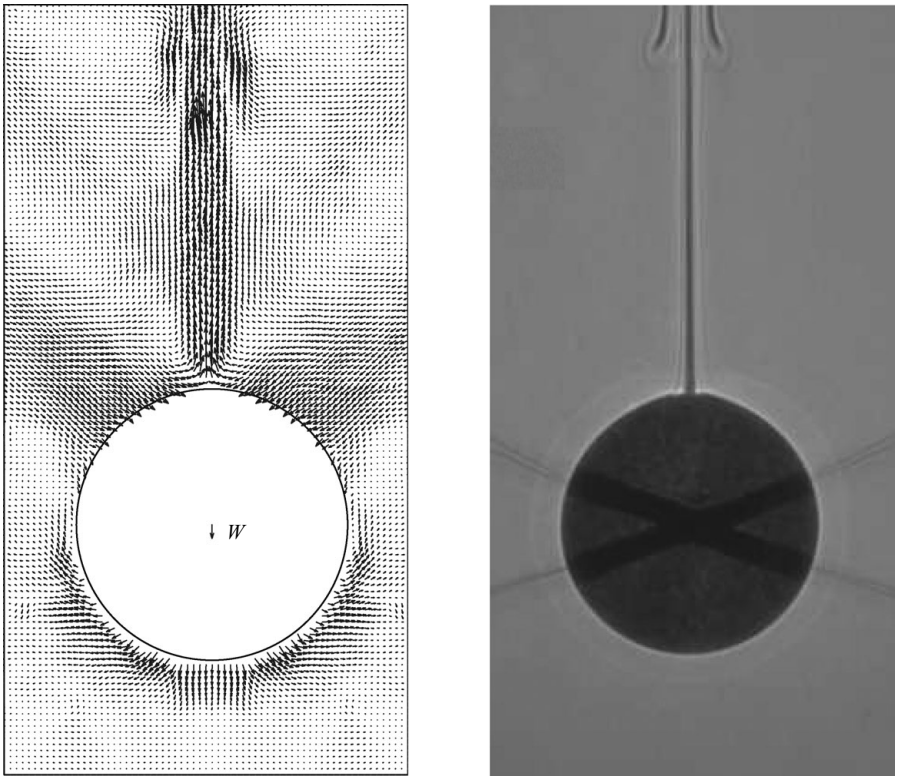

(*a*) (*b*)

FIGURE 11. (*a*) The velocity distributions measured by PIV and (*b*) the shadowgraph image of type A at $(Re, Fr) = (247, 0.32)$. The velocity is depicted in the laboratory frame. The descending velocity of the sphere, W, is given in (*a*) at the centre of the sphere. The vertical laser light sheet comes from the left across the centre of a sphere in (*a*), and the measurement is impossible in the shadow region on the right of the sphere. The velocity vectors in the shadow region are generated using the data on the left side of the sphere, assuming the axisymmetry of the flow.

where H is the total fluid depth. However, this condition is satisfied by none of the type B results in this study for which $a_{max} = 0.5$ cm and $Fr_{max} \sim 10$. Second possibility is that the density difference around the bell-shaped pattern becomes small, and the contrast of the shadowgraph becomes too weak to be discernible. This would occur when the value of N itself is small or when the sphere size a is small and the excited waves have small amplitudes with small density perturbations.

The meandering of jet would disappear simultaneously with the bell-shaped pattern, since the vertical shear between the jet and the downward velocity induced by the internal wave would cause the instability. Considering that the meandering occurs on the central jet and it would be more easily observed than the bell-shaped pattern, it might be a better criterion for the transition between types A and B. However, the meandering of jet disappears precisely on the borderline depicted in figure 4(*a*). We therefore conclude that the present borderline would be a rather definite one, although there are some uncertainties which originate from the values of N and a.

Figure 14 shows the PIV and shadowgraph results for type C at the parameters values of $(Re, Fr) = (1178, 1.50)$, which are very close to the dye visualization

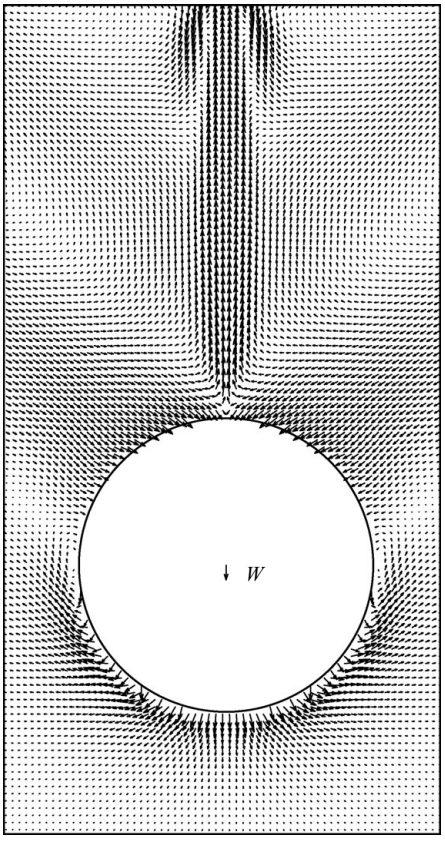

FIGURE 12. The velocity distributions of type A obtained by numerical simulations assuming the axisymmetry of the flow (Hanazaki *et al.* 2009*a*). The parameters are almost the same as figure 11(*a*, *b*), i.e. $(Re,\ Fr) = (247, 0.30)$. The velocity vectors are depicted in the laboratory frame.

(figure 6*b*, $Re = 1189,\ Fr = 1.55$). Similarity of the wake patterns in three measuring methods suggests the near steadiness of the flow. In the velocity distribution (figure 14*a*), a jet broader than type A (figure 11*a*) is actually observed. It would be of interest, albeit a little contradictory, that the vertical velocity in the laboratory frame is not always positive in the jet inferred from the shadowgraph image (figure 14*b*). The velocity is always positive in the moving frame of the sphere so that no recirculation region exists but becomes negative in the laboratory frame near the rear stagnation point of the sphere. An explanation of this phenomenon would be that while the steady non-diffusive flow should be along the density contours because of $\boldsymbol{u} \cdot \nabla \rho = 0$, the contours of total density near the sphere do not go straight up and might give a closed loop, and the contours which are connected to the upper layer would go up outside that closed contour. The closed density contours would appear, since the density or salt concentration is not conserved due to the molecular diffusion of salt, even if it is not so effective as in type A.

The width or diameter of a broad jet in type C increases with the Froude number as could be observed in figure 9. The width is defined here in the shadowgraph images by the distance between the black lines furthest from the centre axis. Since the width changes with height, the width measured at about four diameters from the rear

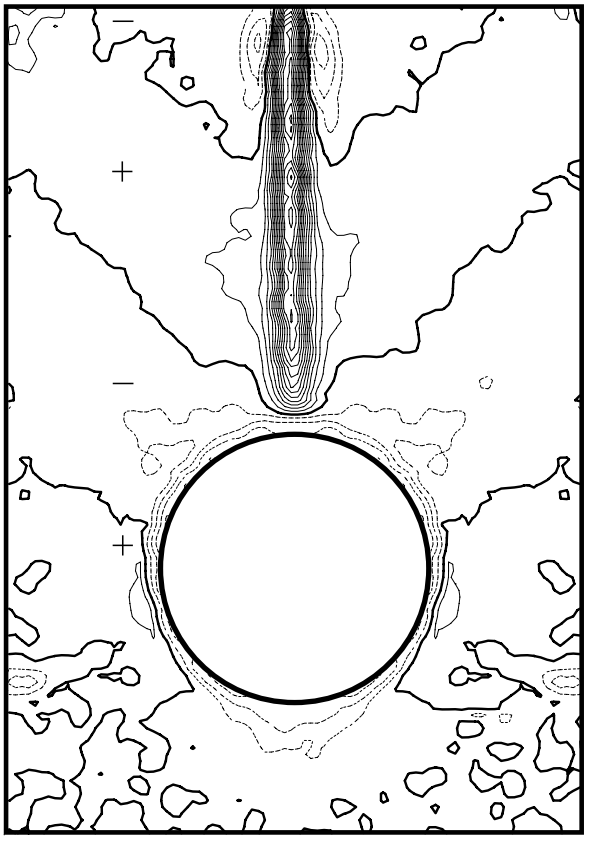

FIGURE 13. Contours of the vertical velocity w in the laboratory frame, obtained by PIV for type A at $(Re, Fr) = (247, 0.32)$. The PIV data are the same as figure 11(a). The bold solid lines denote $w = 0$; the thin solid lines and the + sign denote $w > 0$; and the dashed lines and the – sign denote $w < 0$ with the contour interval of $\Delta w/W = 0.4$.

stagnation point is used as its representative value. Due to this arbitrariness, there are some scatters in the values plotted against $Fr^{1/3}$ in figure 15, which give a relation of $T_C/2a \sim 0.23Fr^{1/3}$. However, the figure shows that the width of broad jet is mainly determined by stratification and not by the Reynolds number or the boundary-layer separation.

In type D ($7 \lesssim Fr \lesssim 16$, $200 \lesssim Re \lesssim 1200$), the generation period of knots or the vertical distance between knots increases with the Froude number as illustrated in figure 16. Indeed, the distance between knots, L_D, is roughly proportional to the Froude number,

$$L_D/2a \sim 0.63Fr, \tag{3.6}$$

as shown in figure 17. On the other hand, the generation period of knots, T_D, and the distance between knots, L_D, have the relation

$$L_D = (W + c)T_D, \tag{3.7}$$

where c (> 0) is the slow ascending velocity of knots in the laboratory frame. If the knots are stationary in the laboratory frame ($c = 0$), the relation reduces to $L_D = WT_D$. Although c slightly increases with time, analysis of a time series of photographs gives

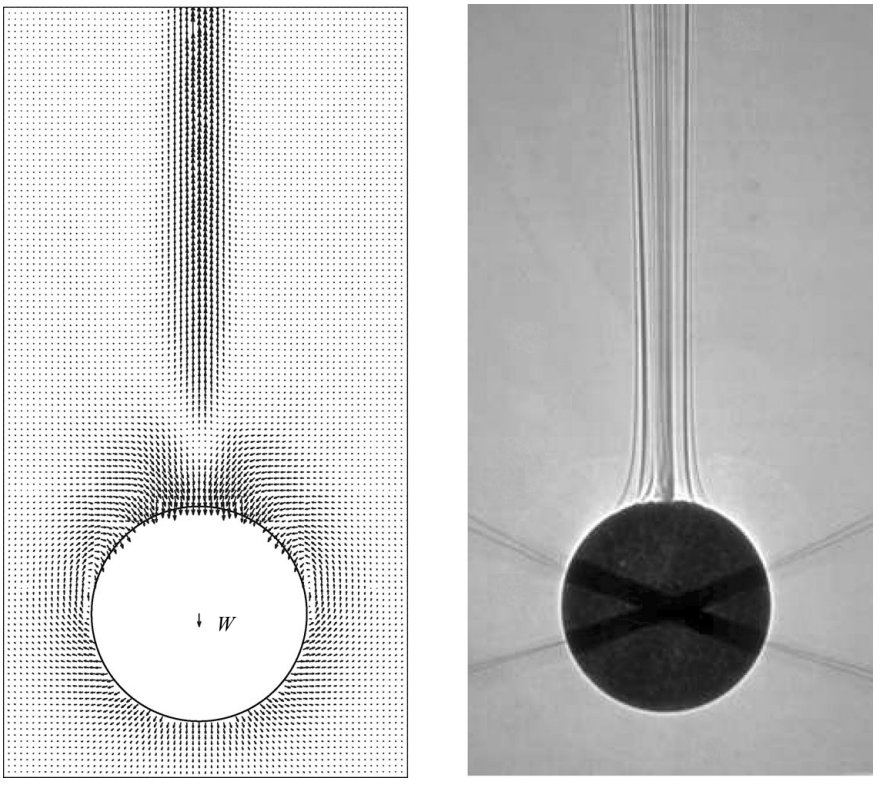

(*a*) (*b*)

FIGURE 14. (*a*) The velocity distributions measured by PIV and (*b*) the shadowgraph image of type C at $(Re, Fr) = (1178, 1.50)$. The velocity is depicted in the laboratory frame. The descending velocity of the sphere, W, is given in (*a*) at the centre of the sphere.

a typical time-averaged value of $c \sim 0.27W$. Combining (3.6) and (3.7) and substituting the experimental value of c, we obtain

$$T_D \sim 1/N. \tag{3.8}$$

Albeit crude approximation, this shows that the generation period of knots is determined by stratification. On the other hand, we know that the oscillation period of internal waves must be larger than $2\pi/N$, about six times larger than that given by (3.8). This suggests that while the generation of knots would be controlled by the density gradient, it is not a direct consequence of internal waves.

In figure 18, shadowgraph images which show the change of distance between knots in type F are presented. Since the moving velocity of knots c_F is generally small compared to the velocity of the sphere ($c_F \lesssim 0.03W$), the distance between knots L_F can be approximated by

$$L_F \sim WT_F, \tag{3.9}$$

where T_F is the generation period of knots. On the other hand, the usual Strouhal number St would be defined using the shedding frequency $f_F (= 1/T_F)$ of an eddy as

$$St = 2af_F/W = 2a/(WT_F). \tag{3.10}$$

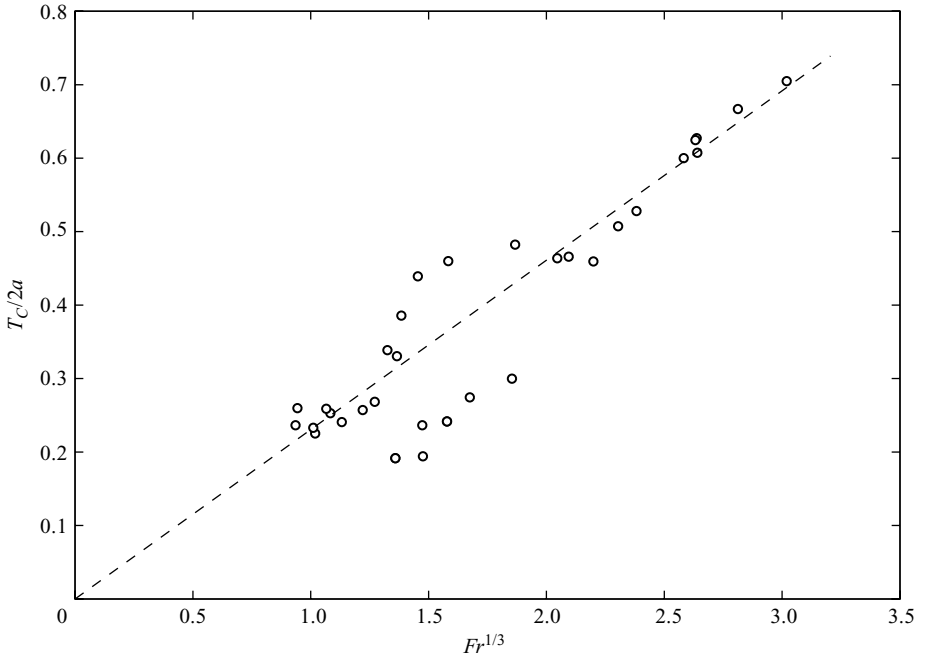

FIGURE 15. Froude-number dependence of the jet diameter T_C in type C. The dashed line denotes $T_C/2a = 0.23Fr^{1/3}$.

Then, the combination of (3.9) with (3.10) gives

$$St \sim 2a/L_F, \tag{3.11}$$

showing that St is the inverse of $L_F/2a$.

Shadowgraph images show that in the parameter range of $400 < Re < 750$ and $33 < Fr < 54$, $L_F/2a$ is generally independent of Re and Fr (figures 18a and 5f) and is determined by

$$L_F/2a = 4.2 \sim 6.6, \tag{3.12}$$

giving $St = 2a/L_F = 0.15 \sim 0.24$. These values agree with the unstratified value $St \sim 0.2$ for a sphere at $Re \sim 400$. At larger Re (> 750) (figure 18b, $Re = 861$), as the wake becomes more turbulent, the Strouhal number increases ($St > 0.3$, i.e. $L_F/2a < 3.3$), again in the same manner as the unstratified fluids which gives $St \sim 1.0$ at $Re = 3 \times 10^3$. These results suggest that the periodic generation of knots in type F essentially corresponds to the vortex shedding in unstratified fluids.

To confirm these processes in type F, we have measured the velocity distributions in the vertical plane across the sphere centre by PIV at the parameters values of $(Re, Fr) = (539, 37.9)$ (figure 19). In laboratory frame, figure 19(a) shows two regions of large horizontal velocity at the top and middle of the figure, which would correspond to the knots observed in the shadowgraph images (figure 18a, b). We note in figure 19(a) that the vertical velocity in the jet of type F is generally 'downward', in contrast to the more strongly stratified cases of types A and C in which the velocity was upward except very near the sphere. This suggests that the apparent jet of type F observed in the shadowgraph is actually reminiscent of the ordinary unstratified wake. Indeed, if we look at the same flow from the frame moving with the sphere

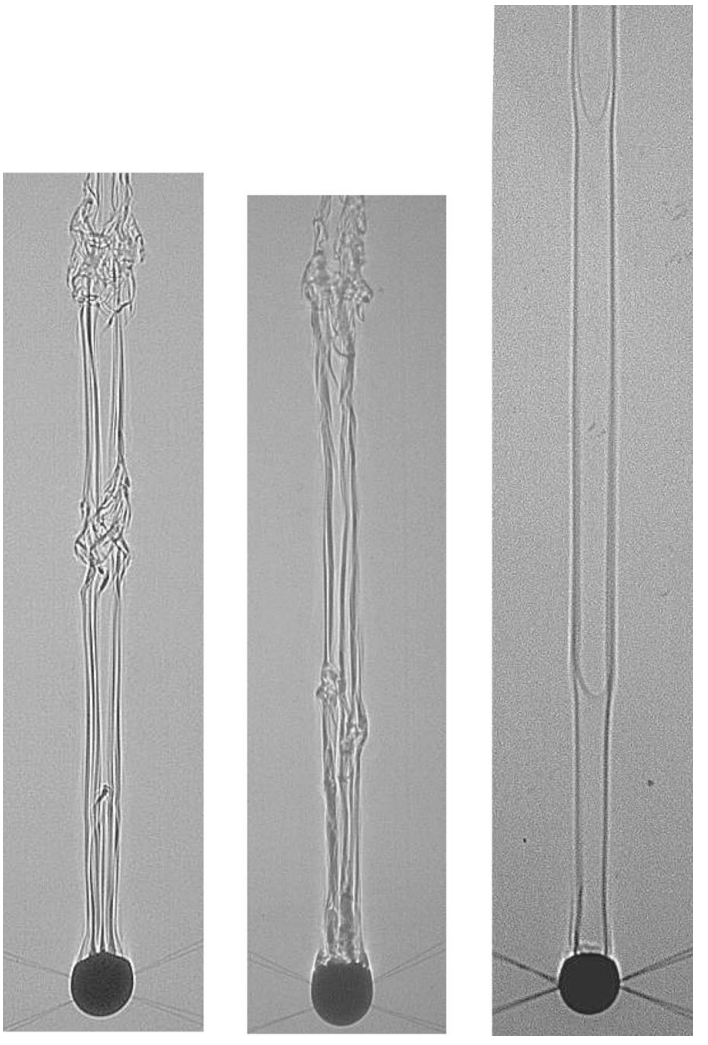

FIGURE 16. Variation of the distance between knots in type D for different Fr. (a) $(Re, Fr) = (678, 7.2)$; (b) $(Re, Fr) = (1185, 9.5)$; (c) $(Re, Fr) = (259, 14.5)$.

(figure 19b), an asymmetric eddy attached to the sphere is observed, and regular wake is observed further downstream. The asymmetric eddy is always on one side of the centre axis of the flow when the sphere is descending in the whole observed area of PIV, whose vertical dimension is about $30a(\sim 3L_F)$ (cf. (3.12)). Then, we can conclude that the eddy would always be on one side during the generation of knots or vortices. This asymmetric vortex shedding is similar to the unstratified flow at $Re \lesssim 500$ (Lee 2000).

The vertical velocity in the jet/wake changes its direction from upward to downward not abruptly but gradually as Fr increases. In type A (figure 11a, $(Re, Fr) = (247, 0.32)$), almost no downward-velocity region is observed, while in type C (figure 14a, $(Re, Fr) = (1178, 1.50)$) such a region appears near the rear stagnation point of the sphere, as already noted. In type D with $(Re, Fr) = (238, 16.7)$, the

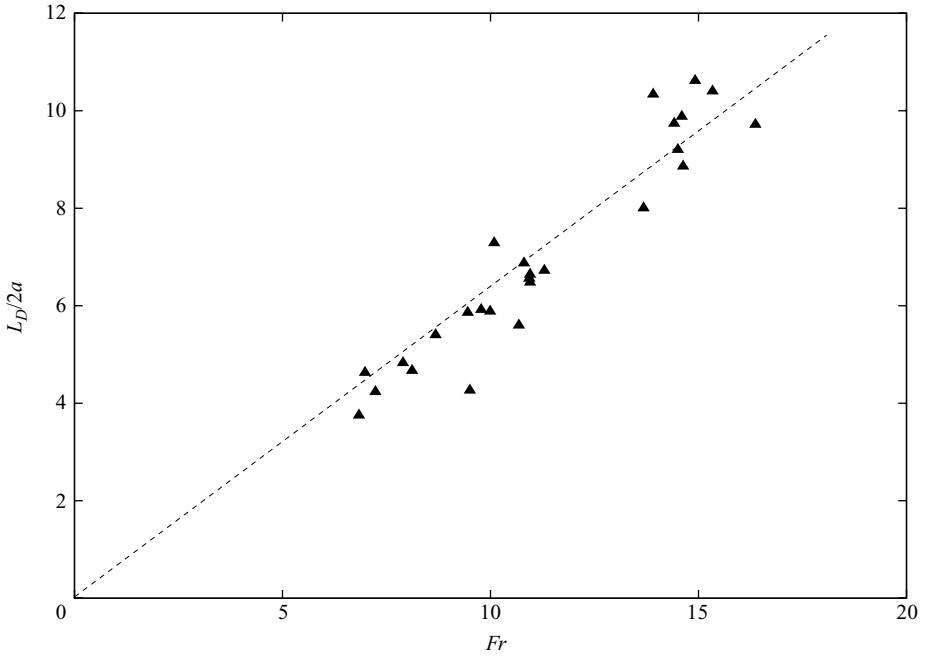

FIGURE 17. Froude-number dependence of the distance between knots in type D. The dashed line denotes $L_D/2a = 0.63Fr$.

upward velocity still exists, but it is observed at a higher position from the sphere, and in type F (figure 19*a*) all the velocities become downward. These results suggest that gradual decrease of buoyancy effects causes the transition from a vertical upward jet to an ordinary wake with the downward velocity in the laboratory frame.

Fluorescent-dye visualization for type F shows that the top view of the spiral structure (not photographed) is elliptic rather than circular, and the knots in type F are generally on only one side of the sphere. For example, all the knots are on the left side in figures 5(*f*) and 18(*a*), while they are at times only on the right side. As the Reynolds number increases, the knots begin to appear on both sides of the sphere as illustrated in figure 18(*b*), and the Strouhal number increases. Vertical distance between those knots decreases to $L_F/2a \sim 2.8$ ($St \sim 0.36$) at $Re \sim 10^3$, and the Strouhal number may further approach a larger unstratified value. However, further increase of Re was not possible in the present experimental apparatus.

4. Conclusions

The wake structure behind a sphere moving vertically at constant speeds in uniformly stratified fluid has been investigated in salt-stratified water, using the shadowgraph technique, fluorescent-dye visualization and PIV. The velocity in the columnar structure observed by the shadowgraph has been measured by PIV, and the existence of a jet has been confirmed. The results have clarified seven types of jet structures, including five new patterns. Many of the characteristics of these patterns, such as the length and width of jets and the generation period of knots, are determined mainly by stratification, except for the case of weak stratification in which the generation of knots is reminiscent of vortex shedding in unstratified fluids.

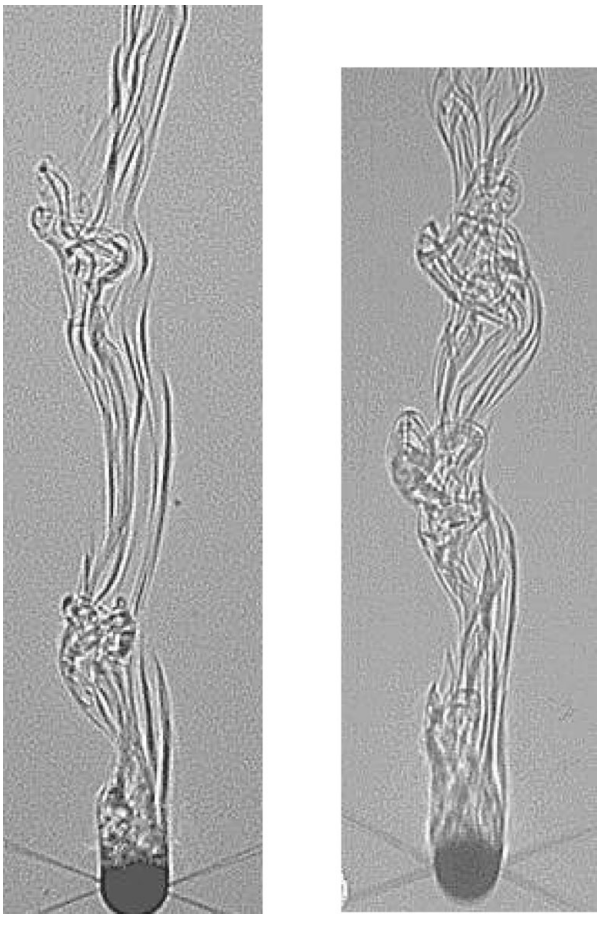

(*a*) (*b*)

FIGURE 18. Variation of the distance between knots in type F for different parameters. (*a*) $(Re, Fr) = (641, 44)$; (*b*) $(Re, Fr) = (861, 52.5)$.

Among others, a bell-shaped structure observed at the upper part of the thin jet has been found to be a disturbance generated by internal waves.

It would be important to note finally that the jet broadens and becomes weaker with decreasing Schmidt number, as has been demonstrated by numerical simulations (Hanazaki *et al.* 2009*b*). This occurs since the density/salt boundary-layer thickness increases, e.g. $\propto Sc^{-1/2}$, and the density contours near the vertical axis simultaneously become sparse, making the buoyancy effects weaker. Therefore, the results reported here would be most conspicuous in the salt-stratified ocean ($Sc = 700$), while they might not be so significant in the temperature-stratified air (Prandtl number $Pr = 0.7$). However, wake structures generated by a vertically moving obstacle cannot be easily inferred from the flows generated by a horizontally moving obstacle and would deserve a further study.

The authors would like to thank Dr Ochoa at CICESE, Mexico, for providing original photographs reported in Ochoa & Van Woert (1977), some of which have been reproduced in Torres *et al.* (2000). In the development of experimental facilities,

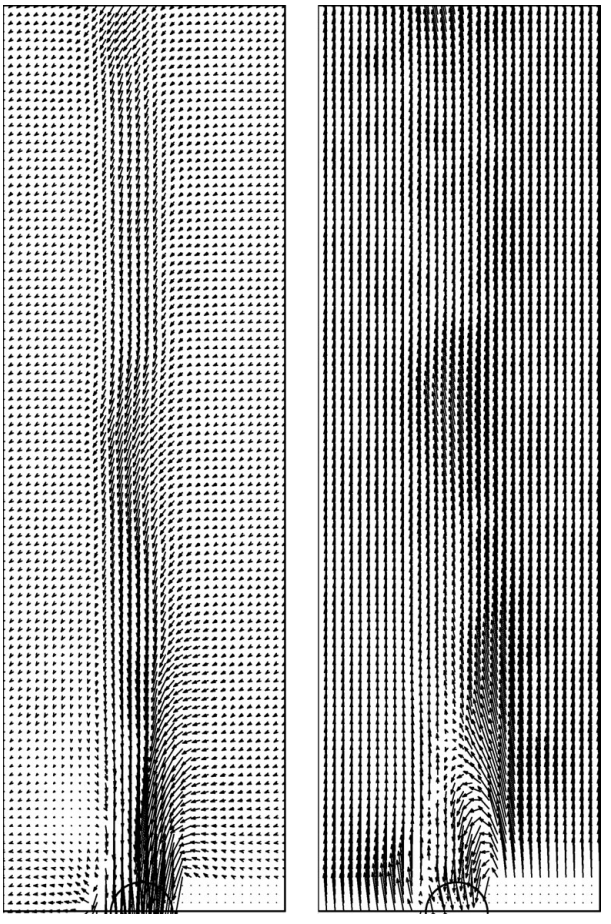

FIGURE 19. The velocity distributions in the vertical plane across the centre of the sphere, which are obtained by PIV for type F at $(Re, Fr) = (539, 37.9)$. (*a*) The elocity in the laboratory frame; (*b*) the velocity in the frame moving with the sphere, obtained by adding the sphere velocity W to the vertical velocity components of figure 19(*a*). The velocity vectors are not depicted in the shadow region on the right of the sphere, since the flow is asymmetric.

the authors would like to sincerely thank Professor T. Karasudani and Mr K. Ishii of Research Institute for Applied Mechanics of Kyushu University and Dr I. Kanda of National Institute for Environmental Studies for many useful and practical advices on the experimental facilities.

REFERENCES

ABAID, N., ADALSTEINSSON, D., AGYAPONG, A. & MCLAUGHLIN, R. M. 2004 An internal splash: levitation of falling spheres in stratified fluids. *Phys. Fluids.* **16**, 1567–1580.

D'ASARO, E. A. 2003 Performance of autonomous Lagrangian floats. *J. Atmos. Ocean. Technol.* **20**, 896–911.

CHOMAZ, J. M., BONNETON, P. & HOPFINGER, E. J. 1993 The structures of the near wake of a sphere moving horizontally in a stratified fluid. *J. Fluid Mech.* **254**, 1–21.

DE SILVA, I. P. D. & FERNANDO, H. J. S. 1998 Experiments on collapsing turbulent regions in stratified fluids. *J. Fluid Mech.* **358**, 29–60.

Hanazaki, H. 1988 A numerical study of three-dimensional stratified flow past a sphere. *J. Fluid Mech.* **192**, 393–419.

Hanazaki, H., Kashimoto, K. & Okamura, T. 2009*a* Structure of jets in the wake of a sphere moving vertically in stratified fluids. In preparation.

Hanazaki, H., Konishi, K. & Okamura, T. 2009*b* Schmidt number effects on the flow past a sphere moving vertically in a stratified diffusive fluid. *Phys. Fluids.* **21**, 026602.

Hunt, J. C. R. & Snyder, W. H. 1980 Experiments on stably and neutrally stratified flow over a model three-dimensional hill. *J. Fluid Mech.* **96**, 671–704.

Lee, S. 2000 A numerical study of the unsteady wake behind a sphere in a uniform flow at moderate Reynolds numbers. *Comp. Fluids* **29**, 639–667.

Lin, Q., Lindberg, W. R., Boyer, D. L. & Fernando, H. J. S. 1992 Stratified flow past a sphere. *J. Fluid Mech.* **240**, 315–354.

McDougall, T. J. 1979 On the elimination of refractive-index variations in turbulent density-stratified liquid flows. *J. Fluid Mech.* **93**, 83–96.

Mowbray, D. E. & Rarity, B. S. H. 1967 The internal wave pattern produced by a sphere moving vertically in a density stratified liquid. *J. Fluid Mech.* **30**, 489–495.

Ochoa, J. L. & Van Woert, M. L. 1977 Flow visualization of boundary layer separation in a stratified fluid. *Unpublished Rep.* Scripps Institute of Oceanography, p. 28.

Spedding, G. R., Browand, F. K. & Fincham, A. M. 1996 The long-time evolution of the initially turbulent wake of a sphere in a stable stratification. *Dyn. Atmos. Ocean.* **23**, 171–182.

Srdić-Mitrović, A. N., Mohamed, N. A. & Fernando, H. J. S. 1999 Gravitational settling of particles through density interfaces. *J. Fluid Mech.* **381**, 175–198.

Torres, C. R., Hanazaki, H., Ochoa, J., Castillo, J. & Van Woert, M. 2000 Flow past a sphere moving vertically in a stratified diffusive fluid. *J. Fluid Mech.* **417**, 217–236.